

# A diagnostic to measure neutral-atom density in fusion-research plasmas

Cite as: Rev. Sci. Instrum. **93**, 093519 (2022); <https://doi.org/10.1063/5.0101683>

Submitted: 02 June 2022 • Accepted: 16 August 2022 • Published Online: 26 September 2022

A. Dogariu,  S. A. Cohen, P. Jandovitz, et al.

## COLLECTIONS

Paper published as part of the special topic on [Proceedings of the 24th Topical Conference on High-Temperature Plasma Diagnostics](#)



View Online



Export Citation



CrossMark

## ARTICLES YOU MAY BE INTERESTED IN

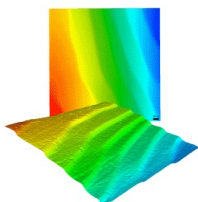
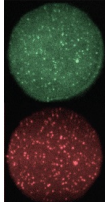
[Upgrade of the helically symmetric experiment Thomson scattering diagnostic suite](#)  
Review of Scientific Instruments **93**, 093518 (2022); <https://doi.org/10.1063/5.0101879>

[Quantifying electron temperature distributions from time-integrated x-ray emission spectra](#)

Review of Scientific Instruments **93**, 093517 (2022); <https://doi.org/10.1063/5.0101571>

[Measurement of electromagnetic waves from runaway electrons](#)

Review of Scientific Instruments **93**, 093516 (2022); <https://doi.org/10.1063/5.0101650>

 <b>MCL</b> MAD CITY LABS INC. <a href="http://www.madcitylabs.com">www.madcitylabs.com</a>	<p>Nanopositioning Systems</p> 	<p>Modular Motion Control</p> 	<p>AFM and NSOM Instruments</p> 	<p>Single Molecule Microscopes</p> 
---	--	--	---	--

# A diagnostic to measure neutral-atom density in fusion-research plasmas

Cite as: Rev. Sci. Instrum. 93, 093519 (2022); doi: 10.1063/5.0101683

Submitted: 2 June 2022 • Accepted: 16 August 2022 •

Published Online: 26 September 2022



View Online



Export Citation



CrossMark

A. Dogariu,<sup>1,2</sup> S. A. Cohen,<sup>3,a)</sup>  P. Jandovitz,<sup>3</sup> S. Vinoth,<sup>3</sup> E. S. Evans,<sup>3</sup>  and C. P. S. Swanson<sup>3</sup> 

## AFFILIATIONS

<sup>1</sup>Mechanical and Aerospace Engineering Department, Princeton University, Princeton, New Jersey 08540, USA

<sup>2</sup>Department of Aerospace Engineering, Texas A&M University, College Station, Texas 77843, USA

<sup>3</sup>Princeton Plasma Physics Laboratory, P.O. Box 451, Princeton, New Jersey 08543, USA

**Note:** This paper is part of the Special Topic on Proceedings of the 24th Topical Conference on High-Temperature Plasma Diagnostics.

<sup>a)</sup>Author to whom correspondence should be addressed: scohen@pppl.gov

## ABSTRACT

A femtosecond two-photon-absorption laser-induced-fluorescence (TALIF) diagnostic was designed, installed, and operated on the Princeton-Field-Reversed Configuration-2 device to provide non-invasive measurements of the time and spatially resolved neutral-atom densities in its plasmas. Calibration of the H<sup>0</sup> density was accomplished by comparison with Kr TALIF. Measurements on plasmas formed of either H<sub>2</sub> or Kr fill gases allowed examination of nominally long and short ionization mean-free-path regimes. With multi-kW plasma heating and H<sub>2</sub> fill gas, a spatially uniform H<sup>0</sup> density of order 10<sup>17</sup> m<sup>-3</sup> was measured with better than ±2 mm and 10 μs resolution. Under similar plasma conditions but with Kr fill gas, a 3-fold decrease in the in-plasma Kr density was observed.

Published under an exclusive license by AIP Publishing. <https://doi.org/10.1063/5.0101683>

## I. INTRODUCTION

Atomic hydrogen (H<sup>0</sup>) plays important roles in magnetic fusion (MFE) devices. H<sup>0</sup> in the hot plasma core, though at a density far less than that of hydrogen ions, dominates several processes, as can be ascertained by evaluation of the continuity,<sup>1,2</sup> momentum conservation,<sup>3</sup> and energy conservation<sup>4</sup> equations.

The edge and divertor plasma of most MFE devices will have quite different plasma parameters than the core, notably 300× lower electron and ion energies, while the neutral density in the divertor is orders-of-magnitude higher than in the core, in cases exceeding 10<sup>20</sup> m<sup>-3</sup>, a regime designed to ameliorate spatially peaked heat loads.<sup>5–7</sup>

H<sup>0</sup> density is essential to several plasma diagnostics including time-of-flight<sup>8</sup> and ion energy analyzers,<sup>9</sup> and high-resolution spectroscopy, as by CPT<sup>10</sup> (coherent population trapping) and DFSS<sup>11</sup> (Doppler-free saturation spectroscopy).

Our approach—and those of an earlier group<sup>12</sup>—to a non-invasive diagnostic for measuring neutral atom densities in MFE devices is to use femtosecond two-photon-absorption laser-induced-fluorescence, fs-TALIF.<sup>13–15</sup> The successful measurements described herein are, in part, due to the Princeton-Field-Reversed

Configuration-2's (PFRC-2's) capability to provide several thousand highly reproducible, multi-ms-duration plasmas per hour, with  $n_e$  to  $5 \times 10^{19}$  m<sup>-3</sup> and electron energies exceeding the keV level.<sup>16</sup>

To display fs-TALIF's suitability for a range of MFE devices, we used either Kr or H<sub>2</sub> fill gases. Due to Kr's larger atomic mass, lower energy (1/40 eV), and larger ionization rate coefficient compared to H<sup>0</sup>, both short and long ionization mean-free-paths (MFP) regimes are accessible. H<sup>0</sup> is created by electron-impact Franck–Condon dissociation while Kr is the fill gas. Accordingly, the H<sup>0</sup> density increases at plasma initiation while Kr's decreases.

Section II describes the apparatus and technique. Section III demonstrates the diagnostic operating on an MFE device. Section IV discusses the results and applicability of fs-TALIF to other MFE research devices.

## II. APPARATUS AND TECHNIQUE

The fs-TALIF method for the detection of H<sup>0</sup> relies on the multi-photon excitation of H<sup>0</sup> by the simultaneous absorption of two 205.08 nm photons, raising H<sup>0</sup> from the ground state to either of the  $3d^2D_{3/2,5/2}$  states, Fig. 1. The laser employed is a pulsed (6 mJ, 100 fs at 1 kHz) Spectra Physics Solstice Ace, tunable 770–830 nm, with harmonics. (The fourth harmonic is

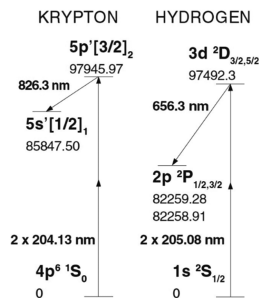


FIG. 1. TALIF-relevant energy levels in Kr<sup>17–19</sup> and H.

at 204 nm.) H- $\alpha$  radiation follows: with an intensity proportional to the ground-state H<sup>0</sup> density. Because the rate coefficients for light absorption by inert gases and hydrogen are well known,<sup>18</sup> absolute calibration of the H<sup>0</sup> density is possible using Kr gas whose density is measured from its pressure. Kr's excitation energy is close to that of L- $\beta$ ; the emission wavelength was accounted for by the spectral response of the detection system. Detection of H- $\alpha$  is performed with a fast (5 ns) camera [PCO Dimax sCMOS camera with LaVision IRO (Intensified Relay Optics) intensifier], viewing transverse to the beam and through a 1 or 10 nm-broad H- $\alpha$  filter. The camera captures images of both the small TALIF-induced H region and the larger nearby region where H- $\alpha$  arises from electron-impact excitation of atoms and dissociative excitation of molecules.

Using fs, pulses allow for two-photon excitation at lower laser energies and without quenching during excitation. Through a translatable FL = 1 m lens, a 30  $\mu$  dia spot size was achieved. The fs-TALIF diagnostic sends a 1 kHz stream of intense UV (centered at 205.08 or 204.13 nm for H and Kr, respectively) laser pulses, each of duration 100 fs and energy up to 0.1 mJ, through PFRC-2 hydrogen or krypton plasma, formed and sustained by up to 100 kW of RF power, here at 4.3 MHz. 27 MHz RF was used at powers below 1 kW.

The LIF emission region,  $\sim$ 20 mm long, was imaged onto the camera using an F/1.2 Nikon lens with a 2 in. diameter, located  $\sim$ 250 mm from the plasma. The camera's response was linear; its 16-bit detector (65 536 counts maximum) was never saturated. The signal count was typically in the range of the low thousands.

The necessity of absorbing two photons makes the emission of the H- $\alpha$  line localized to a volume near the laser beam's focal point, providing excellent spatial resolution of the H<sup>0</sup> density. The position of the diagnosed volume in the PFRC-2 was changed by translating the aforementioned external lens.

The temporal resolution of TALIF is controlled by the timing of the 1 kHz laser pulses relative to events in the plasma. For the highly reproducible, high repetition-rate PFRC-2 plasmas, a time resolution shorter than 10  $\mu$ s was obtained.

The PFRC-2 device, Fig. 2, has an overall length near 2 m. The central vacuum (CC) vessel in which plasma is formed by up to 100 kW of forward RF power,  $P_f$ , (odd-parity rotating magnetic field,  $RMF_o$ ), is a 0.114 m inner-radius Lexan pipe. In these experiments, the power absorbed by the plasma,  $P_a$ , is 20%–60% of  $P_f$ . The magnetic field is produced by axial and nozzle coils and high-temperature-superconductor-filled flux-conserving copper rings, flux-conservings (FCs). For the experiments reported here, the FCs were not superconducting, and the central magnetic field was in the range 100–200 G.

A seed plasma ( $10^{15-17}$  m<sup>-3</sup>),<sup>20</sup> formed at  $z = -1.1$  m by 5–500 W of RF power, flows parallel to the PFRC-2 axis and serves as a target for the higher power  $RMF_o$ . Over much of its operational range, the PFRC-2's  $n_e$  increases with  $RMF_o$  power, applied magnetic field, fill gas pressure, and normalized atomic mass (amu). A 170 GHz interferometer measured a maximum line-integrated electron density of  $10^{19}$  m<sup>-2</sup> with krypton and about 10 $\times$  lower with hydrogen fill gas. Several measurements show the plasma radius to be  $\sim$ 0.04 m, indicating a Kr plasma electron density,  $n_e$ , exceeding  $10^{20}$  m<sup>-3</sup>.

Two TALIF experimental campaigns were held. In the first, the TALIF laser was injected axially, TALIF Beam-1 in Fig. 2, allowing on-axis measurements for  $0.33 < z < 0.37$  m. The TALIF Beam-2 campaign provided radial viewing from  $r = 0$  to 0.08 m, at a distance of 0.05 m from the axial midplane,  $z = 0$ . Both were accomplished by translating a fused-silica lens positioned outside the vacuum chamber, close to the fused-silica entrance window to prevent damage to the window.

Figure 3 shows the decay time,  $\tau_{Kr}$ , of the Kr 826.3 nm line with no plasma and that for H- $\alpha$  fluorescence,  $\tau_H$ , with plasma.  $\tau_{Kr} = 29$  ns is close to the decay rate coefficients of the excited Kr  $3d^2D_{3/2,5/2}$  states (29.8 and 32.5 ns). Figure 4 shows the brightness and spatial extent of the Kr line at 5 ns after the TALIF laser pulse. Similar decay times and spatial profiles of the TALIF-induced brightness during high power  $RMF_o$  discharges demonstrate the expected lack-of-quenching of the  $3d^2D_{3/2,5/2}$  states in PFRC-2 plasmas; similarly, no change in  $\tau_{Kr}$  or spatial profile was observed at fill pressures to 100 mTorr, corroborating the technique under these conditions. Based on these measurements, the spatial resolution is less than 50  $\mu$  in the beam-transverse ( $y$ -axis) direction and  $\pm$ 2 mm in the beam-parallel ( $x$ -axis) direction. At lower laser intensity, the fluorescence signal at 826.3 nm was linear with Kr pressure and

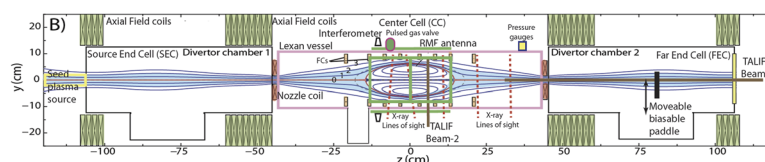
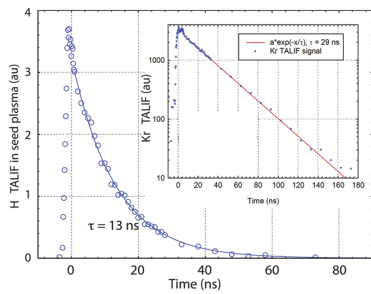
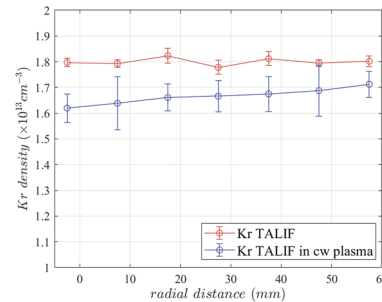


FIG. 2. Schematic of the PFRC-2. The approximate locations of several diagnostics are shown. The PFRC-2 has three sections: the source end cell (SEC), center cell (CC), and far end cell (FEC). The CC contains eight co-axial passive high-temperature-superconductor-filled copper rings labeled FCs. Three (North, Top, and Bottom) of the four  $RMF_o$  antennae are shown in green. The TALIF beam may be directed axially, Beam-1, or transversely, Beam-2. The location of the focal point is controlled by an external lens.



**FIG. 3.**  $H^{\circ}$  (656 nm) and Kr fluorescence (826 nm) vs time after the TALIF laser pulse,  $t = 0$ . The measured signal decay times match the predicted values intensifier gate time 1 ns. Kr: no plasma.  $H^{\circ}$ : in seed plasma.



**FIG. 5.** Kr density vs radius, with and without seed plasma: Fill pressure 0.55 mT. Blue—with plasma ( $P_{RF} = 240$  W); Red—no plasma ( $P_{RF} = 0$  W).  $B(0,0) = 145$  G.

quadratic with the laser power. (No sign of quenching was seen in  $H^{\circ}$  experiments.)

### III. DEMONSTRATION OF THE DIAGNOSTIC

Time-dependent, radially resolved Kr, and  $H^{\circ}$  densities were measured in both the tenuous low-power RF seed plasma and the denser higher power  $RMF_o$ -heated plasma.

#### A. Kr density

In the TALIF Beam-2 campaign, data were accumulated for each of eight focal points, corresponding to eight radial positions along the same chord. Figure 5 shows results from a seed plasma formed by 240 W of 27 MHz with  $n_e \sim 10^{17} \text{ m}^{-3}$  and  $T_e \sim 5$  eV. The seed plasma column was 0.12 m in diameter at the PFRC-2 midplane and reduced in size toward the nozzle coils, with the profile set by the ratio of the magnetic field created by the nozzle coils to that created by the axial field coils, the distance from the midplane, and the diameter of the nozzle coil's orifice. A 10% decrease in Kr density at  $r = 0$  occurs when the seed plasma is formed and 5% at  $r = 0.06$  m, which is near the seed plasma's edge.

The Kr density was measured in 10 ms-duration,  $RMF_o$ -heated plasmas formed at  $P_f = 17$  kW,  $P_a = 7.6$  kW, 1.05 mT fill pressure, and  $B(0,0) = 160$  G. The plasma showed no MHD oscillations and had a nearly constant  $n_e \sim 6 \times 10^{18} \text{ m}^{-3}$  throughout the discharge. Figure 6 shows the Kr density vs time at four radial positions. The  $RMF_o$  strength,  $B_{RMF}$ , had a maximum of 7 G at the PFRC-2's z axis. At each radius, the Kr density falls at the start of the

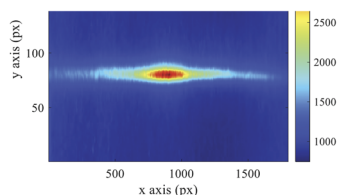


**FIG. 4.** Spatial profile of Kr fluorescence at  $t = 5$  ns. The x axis is parallel to the TALIF beam and the y axis is perpendicular. 1 mm = 18 px. The units of the color scale are counts per pixel (px).

10 ms-duration discharge and remains near that level for the entire 10 ms. At the termination of the discharge, a rise in Kr density above the fill level is seen, most prominently at  $r = 29$  mm; it decays with a 5 ms characteristic time. During the application of  $RMF_o$ , the Kr density remains highest near the plasma edge,  $r = 40$  mm, and falls by 60% near the plasma center, at  $r \sim 8$  mm.

The fast-camera-equipped TALIF spectrometer also detects the electron-impact-induced radiation, see Fig. 7, from the same Kr transition as the TALIF. When  $RMF_o$  was applied, the electron-impact-excitation radiation of Kr increased a factor of 15–30 above the seed-plasma value and stayed nearly constant for the duration of the  $RMF_o$  pulse. Immediately after the discharge ended, the emission fell to 50% of its pre-discharge value and then recovered in 1 ms.

#### B. $H^{\circ}$ density

Figure 8 shows the  $H^{\circ}$  density vs time at  $r = 40$  mm in a 5.8 ms-duration  $RMF_o$ -heated discharge initiated at  $t = 3.7$  ms. (The data represent an average of  $\sim 100$  discharges.) During this experiment, the plasma exhibited a 15 kHz,  $m = 1$  rotating mode, with  $\sim 20$  mm displacement. Accordingly, the TALIF-measured density is an average. The temporal resolution was 20  $\mu\text{s}$  at the beginning and end of the discharge. Figure 9 is the temporal evolution of the plasma  $H\text{-}\alpha$  emission along a line-of-sight tangential to  $r = 40$  mm. A large difference is seen after the termination of the  $RMF_o$  power: the plasma emission falls in 20  $\mu\text{s}$  while the  $H^{\circ}$  density exponentially decays with a characteristic time of 400  $\mu\text{s}$ .

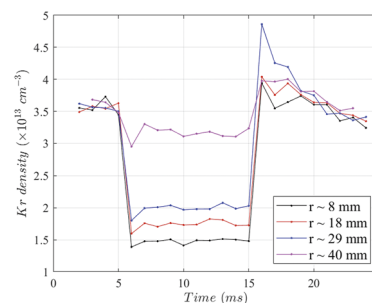


**FIG. 6.** Ground-state Kr density vs time at four radial locations,  $r = 8, 18, 29,$  and  $40$  mm, with  $RMF_o$  power applied at  $t = 5$  ms.

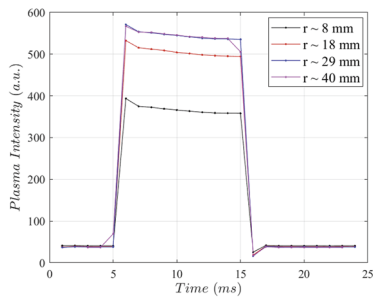


**FIG. 7.** Line-average Kr emission vs time caused by electron-impact excitation. The four positions are the same as in Fig. 6.

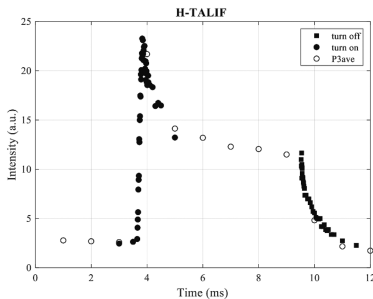


**FIG. 8.** TALIF H- $\alpha$  signal (arb units) at  $r = 40$  mm vs time for (identical)  $RMF_o$ -heated discharges ( $P_f \sim 60$  kW). The maximum  $H^0$  density is  $2 \times 10^{17} \text{ m}^{-3}$ . The non-zero  $H^0$  density before and after  $RMF_o$  is due to the seed plasma.  $RMF_o$  power applied between 3.7 and 9.5 ms.

#### IV. DISCUSSION

Use of Kr and  $H_2$  fill gases in the PFRC-2 allows access to plasmas that are either opaque or transparent to neutrals, with contributing factors being the relatively high ionization rate coefficient of Kr,<sup>21,22</sup> and the higher plasma density achievable with Kr. In addition, Kr's greater mass and lower energy than  $H^0$  significantly shorten the ionization mean-free-path ( $\lambda_i$ ). The net effect of the latter two is (room-temperature) Kr having a velocity lower than (Franck-Condon)  $H^0$ 's by a factor near 80. The  $\lambda_i$  for 1/40 eV Kr is about 1 mm at  $T_e = 10$  eV and  $n_e = 6 \times 10^{18} \text{ m}^{-3}$ .

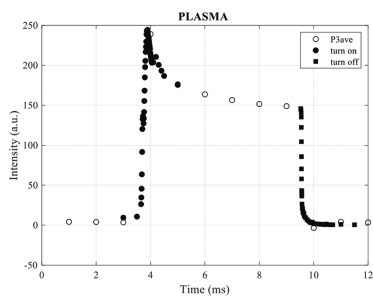


**FIG. 9.** Plasma electron-impact-induced H- $\alpha$  emission (arb units) vs time for the same  $RMF_o$ -heated discharges as in Fig. 8 ( $P_f \sim 60$  kW).

#### A. Kr density

With no plasma, the TALIF-measured Kr density was 7.5% less than that evaluated from the baratron-measured pressure, a difference attributable to impurity gases, primarily  $H_2O$ , in the Lexan chamber.

For the Kr seed plasma, the predicted  $\lambda_i$  for 1/40 eV Kr is  $180 \pm 90$  mm; a  $20 \pm 10\%$  Kr density drop from the Lexan vessel inner wall toward the z axis, about a factor of 2 more than shown in Fig. 5. A 20% lower  $T_e$  would place the predicted density within the error bars shown in Fig. 5. Note that at fill pressures below 1 mT and RF heating power above 50 W, a small percentage, <1%, of the plasma electrons have high energy,<sup>16</sup> with an effective temperature of 200–3000 eV. The temperature of this minority population increases as the fill pressure is lowered. At the 1% level, these warm electrons would increase the effective ionization rate by up to 20% for bulk  $T_e = 5$  eV and by 100% for  $T_e = 4$  eV.

$RMF_o$ -heated Kr plasmas have  $n_e$  to  $5 \times 10^{19} \text{ m}^{-3}$  and  $T_e$  to 50 eV. For the experiments described here,  $n_e = 10^{19} \text{ m}^{-3}$ , the plasma radius was near 0.05 m, and  $T_e = 10$  eV. For 1/40 eV Kr, these result in  $_{Kr}\lambda_i$  less than 1 mm and an ionization time of  $_{Kr}\tau_i = (n_e \lambda_i \langle \sigma v \rangle_i)^{-1} = 5 \mu\text{s}$ , where  $_{Kr}\langle \sigma v \rangle_i$  is the Maxwellian-averaged ionization rate coefficient of Kr by electron impact.<sup>23,24</sup> This ionization time is consistent with the rate of density rise when the  $RMF_o$  power is first applied.

Thus, Fig. 6 is indeed surprising in that it shows the Kr density only falling 60% from the plasma edge to near the z axis. We are considering a number of potential causes. These will be discussed in the future papers.

The electron-impact-induced Kr radiation, Fig. 7, is highest for the lines-of-sight tangent to  $r = 4\text{--}6$  cm. For an isothermal plasma, this indicates that the product of the electron density and the neutral density is hollow on axis. The electron-impact-induced radiation immediately after  $RMF_o$  cessation shows a dip below the pre-discharge value. This and other data show that loss of seed plasma occurs when the  $RMF_o$  is shut off.

The above observations imply that radial plasma losses dominate the particle transport, hence the particle confinement is as in limiter tokamaks, high recycling off the inner wall (limiter) components. Additional evidence supporting this interpretation is (1) the ion confinement time being comparable to  $r_s/c_s$  as well as Bohm transport evaluated with  $T_e = 10$  eV; (2) pressure gauges in the FEC and SEC did not show a detectable pressure rise (<1%) during by the  $RMF_o$  pulses; (3) electrostatic probes near the Lexan vessel's inner wall measure large currents during  $RMF_o$ ; and (4) at 3 eV,  $Kr^+$  has a gyro-radius of >100 mm at the magnetic field used in these experiments. Radiation losses<sup>25</sup> become increasingly important as  $n_e$  and  $T_e$  rise, reaching  $1 \text{ W cm}^{-3}$  at  $10^{19} \text{ m}^{-3}$  and 10 eV. Energy loss by CX is negligible.

#### B. $H^0$ density

The radial profile of the  $H^0$  density was independent of the radius but varied with time. The flat profile is consistent with the smaller ionization rate coefficient compared with Kr, the lower plasma density of hydrogen plasmas, and the relatively high speed of the Franck-Condon-created  $H^0$  neutrals. The calculated penetration of  $H_2$  into these plasmas is near 10 mm. Based on the above, the ratio of atomic to molecular hydrogen densities is >10:1 in

the plasma core. The low on-axis  $H^0$  and  $H_2$  densities translate to  $\tau_p \sim (n_n \langle \sigma v \rangle_i)^{-1} \sim 0.5$  ms. The transit time of  $H^0$  across the CC vessel is  $100 \mu\text{s}$  at  $1/40$  eV and  $10 \mu\text{s}$  at 2 eV.  $H^0$  should thermalize with the Lexan wall or BN (boron nitride) covered FCs in a few bounces. Several bounces of the  $H^0$  and residence on the walls are necessary to recombine to  $H_2$ . The decay of the  $H^0$  density after termination  $RMF_0$  power is  $\sim 0.4$  ms, implying that four bounces of thermal  $H^0$  are required for recombination.

### C. Range and applicability of fs-TALIF to other MFE devices

To avoid electron-induced excitation overshadowing TALIF's photon excitation, the electron density must be less than  $10^{22} \text{ m}^{-3}$ . Tokamaks, stellarators, mirror machines, dipoles, and steady-state FRCs generally satisfy this criterion, while Z-pinch, plasma foci, and pulsed FRCs do not. The plasma must be optically thin to the emitted radiation, hence the neutral  $H^0$  density must be below  $\sim 10^{22} \text{ m}^{-3}$ , a criterion also satisfied in the cores of tokamaks, stellarators, mirror machines, dipoles, and steady-state FRCs. This criterion may not be satisfied in their divertor regions, giving reason to use fs-TALIF there, to test models. The minimum detectable  $H^0$  density depends on the integration time. On the PFRC-2, that minimum was  $10^{15} \text{ m}^{-3}$  for a single laser pulse. There are many factors that affect the minimum, an important one being the proximity of the detector to the MFE device. Highly radioactive devices would need to have the detector at least 3 m from the plasma edge, reducing the  $H\text{-}\alpha$  flux more than  $100\times$  compared with the PFRC-2.

### V. SUMMARY

In this paper, we demonstrated that fs-TALIF can provide spatially, to  $\pm 2$  mm, and temporally resolved, to  $10 \mu\text{s}$ , measurement of the density of certain previously inaccessible atoms, e.g.,  $H^0$ . The first measures of  $H^0$  and Kr time-dependent profiles within fusion-relevant plasmas were presented. That Kr density in the plasma was much higher than expected motivates further experimentation and modeling.

### ACKNOWLEDGMENTS

This work was performed under DOE Contract No. DE-AC02-09CH11466 using resources of the Princeton Collaborative Low Temperature Plasma Research Facility (PCRF <http://pcrf.ppl.gov>) and ARPA-E Award No. DE-AR0001099 (Princeton Fusion Systems). We are grateful to Y. Raites, M. Paluszek, and S. Thomas for their encouragement and support and to B. Berlinger and C. Brunkhorst for their excellent technical work.

### AUTHOR DECLARATIONS

#### Conflict of Interest

The authors have no conflicts to disclose.

### Author Contributions

**A. Dogariu:** Conceptualization (equal); Data curation (lead); Formal analysis (lead); Funding acquisition (lead); Investigation (lead); Methodology (lead); Project administration (equal); Resources (equal); Software (lead); Supervision (equal); Visualization (lead); Writing – original draft (equal); Writing – review & editing (equal). **S. A. Cohen:** Conceptualization (equal); Funding acquisition (equal); Investigation (equal); Project administration (equal); Supervision (equal); Writing – original draft (lead); Writing – review & editing (lead). **P. Jandovitz:** Investigation (supporting); Resources (supporting). **S. Vinoth:** Investigation (supporting); Resources (supporting). **E. S. Evans:** Data curation (supporting); Investigation (supporting); Resources (supporting). **C. P. S. Swanson:** Data curation (supporting); Investigation (supporting); Resources (supporting).

### DATA AVAILABILITY

The data that support the findings of this study are openly available at <http://arks.princeton.edu/ark:/88435/dsp01x920g025r>.<sup>26</sup>

### REFERENCES

- 1 J. D. Strachan et al., *Nucl. Fusion* **22**, 1145 (1982).
- 2 S. A. Cohen, "Particle confinement in fusion devices," in *Physics of Plasma-Wall Interactions in Controlled Fusion*, edited by D. E. Post and R. Behrisch (NATO ASI Series, **1980**), Vol. 62, p. 73.
- 3 A. L. Hoffman, *Nucl. Fusion* **43**, 1091 (2003).
- 4 M. F. A. Harrison, "Atomic physics in fusion devices," in *Physics of Plasma-Wall Interactions in Controlled Fusion*, edited by D. E. Post and R. Behrisch (NATO ASI Series, **1980**), Vol. 62, p. 281.
- 5 M. Petracic, D. Post, D. Heifetz, and J. Schmidt, *Phys. Rev. Lett.* **48**, 326 (1982).
- 6 W. L. Hsu et al., *Phys. Rev. Lett.* **49**, 1001 (1982).
- 7 G. F. Matthews, *J. Nucl. Mater.* **220**, 104 (1995).
- 8 D. E. Voss and S. A. Cohen, *J. Nucl. Mater.* **93–94**, 405 (1980).
- 9 R. Kaita et al., *Nucl. Fusion* **26**, 863 (1986).
- 10 D. R. Farley, J. M. Mitrani, and S. A. Cohen, *Phys. Plasmas* **85**, 033412 (2012).
- 11 A. Zafar, E. Martin, and S. Shannon, *Rev. Sci. Instrum.* **89**, 10D126 (2018).
- 12 R. M. Magee et al., *Rev. Sci. Instrum.* **83**, 10D701 (2012).
- 13 J. Bokor et al., *Phys. Rev. A* **24**, 612 (1981).
- 14 A. Dreizler and B. Böhm, *Proc. Combust. Inst.* **35**, 37 (2015).
- 15 J. Amorim, G. Baravian, and J. Jolly, *J. Phys. D: Appl. Phys.* **33**, R51 (2000).
- 16 C. Swanson and S. A. Cohen, *Phys. Plasmas* **26**, 060701 (2019).
- 17 J. Han and M. C. Heaven, *Opt. Lett.* **40**, 1310 (2015).
- 18 K. Niemi, V. Schulz-von der Gathen, and H. F. Döbele, *J. Phys. D: Appl. Phys.* **34**, 2330 (2001).
- 19 V. L. Sukhorukov, I. D. Petrov, B. M. Lagutin, A. Ehresmann, K. H. Schartner, and H. Schmoranzler, *Phys. Rep.* **786**, 1 (2019).
- 20 P. Jandovitz et al., *Phys. Plasmas* **25**, 030702 (2018).
- 21 L. J. Kieffer and G. H. Dunn, *Rev. Mod. Phys.* **38**(1), 1 (1966).
- 22 A. A. Sorokin, L. A. Shmaenok, S. V. Bobashev, B. Mobus, M. Richter, and G. Ulm, *Phys. Rev. A* **61**, 022723 (2000).
- 23 A. Kobayashi, G. Fujoki, A. Okaji, and T. Masuoka, *J. Phys. B: At., Mol. Opt. Phys.* **35**, 2087 (2002).
- 24 S. D. Loch et al., *Phys. Rev. A* **66**, 052708 (2002).
- 25 D. E. Post, R. V. Jensen, C. B. Tarter, W. H. Grasberger, and W. A. Lokke, *At. Data Nucl. Data Tables* **20**, 397 (1977).
- 26 See <http://arks.princeton.edu/ark:/88435/dsp01x920g025r> for the data that support the findings of this study.